

# Template free synthesis of $\text{LiV}_3\text{O}_8$ nanorods as a cathode material for high-rate secondary lithium batteries

Anqiang Pan,<sup>ab</sup> Jun Liu,<sup>\*c</sup> Ji-Guang Zhang,<sup>\*b</sup> Guozhong Cao,<sup>d</sup> Wu Xu,<sup>b</sup> Zimin Nie,<sup>b</sup> Xiao Jie,<sup>b</sup> Daiwon Choi,<sup>b</sup> Bruce W. Arey,<sup>e</sup> Chongmin Wang<sup>e</sup> and Shuquan Liang<sup>\*a</sup>

Received 25th August 2010, Accepted 12th October 2010

DOI: 10.1039/c0jm02810j

A novel, template-free, low-temperature method has been developed to synthesize  $\text{LiV}_3\text{O}_8$  cathode material for high-power secondary lithium (Li) batteries. The  $\text{LiV}_3\text{O}_8$  prepared using this new method was characterized by X-ray diffraction (XRD), scanning electron microscopy (SEM), and transmission electron microscopy (TEM). The thermal decomposition process was investigated using thermogravimetric (TG) and differential thermal analysis (DTA).  $\text{LiV}_3\text{O}_8$  produced using the conventional high-temperature fabrication method also was analyzed. The electrochemical performances and the effects of synthesis temperature on our  $\text{LiV}_3\text{O}_8$  and the conventionally produced  $\text{LiV}_3\text{O}_8$  were compared. The  $\text{LiV}_3\text{O}_8$  produced using our new method has a nanorod crystallite structure composed of uniform, well-separated particles with diameters ranging from 30 to 150 nm. The TEM work reveals the stacking defaults within the nanorod structures, which would facilitate the electron transportation during the insertion and removal process of lithium ions. It delivers specific discharge capacities of 320  $\text{mAh g}^{-1}$  and 239  $\text{mAh g}^{-1}$  at current densities of 100  $\text{mA g}^{-1}$  and 1  $\text{A g}^{-1}$ , respectively. It also exhibits excellent capacity retention with only 0.23% capacity fading per cycle. This excellent electrochemical performance can be attributed to the superior structural characteristics of our material, and the results of our study demonstrate that  $\text{LiV}_3\text{O}_8$  nanorod crystallites produced by this new thermal decomposition method are promising cathode materials for high-power Li batteries.

## 1. Introduction

Rechargeable  $\text{Li}^+$ -ion batteries are widely used in commercial electronic devices, and because of their higher energy density and longer life cycle, they also are being considered for high-power applications such as electric vehicles.<sup>1</sup> Although  $\text{LiCoO}_2$  is the state-of-the-art cathode material for  $\text{Li}^+$ -ion batteries used in portable electronics, it has drawbacks, such as its high cost, the relative toxicity of cobalt, and safety concerns arising from overcharging of the material. Thus, other intercalation materials such as Li metal phosphates are being studied extensively as alternative cathode materials for  $\text{Li}^+$ -ion batteries.<sup>2–5</sup> During the last 30 years,  $\text{Li}_{1+x}\text{V}_3\text{O}_8$  has been investigated extensively as a cathode material because of its higher specific capacity, lower cost, and better safety features.<sup>6–8</sup> The monoclinic structure of  $\text{Li}_{1+x}\text{V}_3\text{O}_8$ <sup>9</sup> consists of  $(\text{V}_3\text{O}_8)^-$  layers oriented along the *a* axis, pinned together by  $\text{Li}^+$  ions at the octahedral sites in the interlayer. The excess Li corresponding to the amount *x* involved in the charge/discharge processes is accommodated at the tetrahedral

sites in the interlayers.<sup>10,11</sup>  $\text{Li}^+$  ions residing in octahedral sites before Li insertion act as a ‘pin’ for the layers and do not hinder the incoming  $\text{Li}^+$  ions from occupying empty tetrahedral sites.<sup>12</sup>  $\text{Li}_{1+x}\text{V}_3\text{O}_8$  exhibits good structural reversibility during the charge/discharge processes, and despite its structural advantages, its electrochemical performance has been found to be influenced by the method used to synthesize the material.<sup>7,10,13–17</sup> Conventional synthesis of  $\text{Li}_{1+x}\text{V}_3\text{O}_8$  by solid-state reaction of  $\text{Li}_2\text{CO}_3$  and  $\text{V}_2\text{O}_5$  at 680 °C for 10 h requires a large amount of thermal energy and a long reaction time. In addition, it is difficult to accurately control the Li : vanadium(v) ratio because the Li sources evaporate. The specific capacity of  $\text{Li}_{1+x}\text{V}_3\text{O}_8$  prepared by this method also is low.<sup>12</sup> Many other methods such as a sol–gel process,<sup>18–20</sup> a hydrothermal process,<sup>21,22</sup> freeze-drying,<sup>7,23</sup> spray drying,<sup>24,25</sup> a rheological phase reaction method,<sup>26</sup> an ultrasonic method,<sup>27,28</sup> a flame pyrolysis method,<sup>29</sup> a low-heating solid-state method,<sup>30</sup> microwave sol–gel method,<sup>31,32</sup> the (EDTA) sol–gel method,<sup>33</sup> and a surfactant-assisted polymer precursor method<sup>10</sup> have been used to synthesize  $\text{LiV}_3\text{O}_8$ . However, the rate performances of  $\text{Li}_{1+x}\text{V}_3\text{O}_8$  cathodes prepared by these methods are not satisfactory.

As is well known, the kinetic diffusion of  $\text{Li}^+$  ions into  $\text{LiV}_3\text{O}_8$  tetrahedral sites is of great importance to the electrochemical performance of the material. Reducing the particle size would shorten the  $\text{Li}^+$ -ion diffusion distance and increase the surface contact area between the electrode and electrolyte. Therefore, reducing the particle size may lead to higher specific capacities and better rate performances of these materials. In addition, the free expansion of the nanoparticles during  $\text{Li}^+$ -ion intercalation

<sup>a</sup>Department of Materials Science and Engineering, Central South University, Changsha, Hunan, 410083, China. E-mail: lsq@mail.csu.edu.cn

<sup>b</sup>Energy and Environment Directorate, Pacific Northwest National Laboratory, Richland, WA, 99354, USA. E-mail: jiguang.zhang@pnl.gov

<sup>c</sup>Fundamental and Computational Science Directorate, Pacific Northwest National Laboratory, Richland, WA, 99354, USA. E-mail: jun.liu@pnl.gov

<sup>d</sup>Department of Materials Science and Engineering, University of Washington, Seattle, WA, 98195, USA

<sup>e</sup>Environmental Molecular Sciences Laboratory, Pacific Northwest National Laboratory, Richland, WA, 99354, USA

would lower the kinetic barrier for Li<sup>+</sup>-ion diffusion. For practical applications, a facile, fast fabrication method that could be carried out at low-temperatures would be preferred by manufacturers.

In this paper, we describe a novel, low-temperature, cost-effective method to synthesize LiV<sub>3</sub>O<sub>8</sub> nanorods using thermal co-decomposition of V and Li precursor mixtures at various temperatures in air for 2 hours, where the precursor mixtures are produced by a liquid method. The morphology, crystal structure, and electrochemical properties of the synthesized LiV<sub>3</sub>O<sub>8</sub> nanorods synthesized at different temperatures are evaluated by various methods. The high capacities, good capacity retentions, and power performances of our novel synthesized LiV<sub>3</sub>O<sub>8</sub> electrodes are documented in this paper.

## 2. Experimental

All chemicals used in our study were analytical grade and were used as received without further purification. V<sub>2</sub>O<sub>5</sub>, CH<sub>3</sub>COO-Li·2H<sub>2</sub>O, and oxalic acid (H<sub>2</sub>C<sub>2</sub>O<sub>4</sub>) were used to prepare the precursor solution; the oxalic acid was used as both a chelating and a reducing agent. First, V<sub>2</sub>O<sub>5</sub> and oxalic acid in a stoichiometric ratio of 1 : 3 were dissolved in actively stirred deionized water at room temperature until a clear blue solution was formed. Next, a stoichiometric amount of CH<sub>3</sub>COOLi·2H<sub>2</sub>O was added, and the mixture was vigorously stirred for one hour, and the resulting solution was heated overnight in an oven at 80 °C. The as-obtained material was calcined at 350 °C, 400 °C, and 500 °C in air for 2 h, and the samples obtained were designated LT350, LT400, and LT500. For comparison, LiV<sub>3</sub>O<sub>8</sub> was also prepared using the conventional solid-state method. V<sub>2</sub>O<sub>5</sub> powder and solid Li<sub>2</sub>CO<sub>3</sub> were the starting reagents, and the mixture was calcined at 680 °C for 10 h (this sample was designated HT680).

The crystalline structures of the prepared samples were determined by X-ray diffraction (XRD) using a Scintag XDS2000  $\theta$ - $\theta$  powder diffractometer equipped with a Ge (Li) solid-state detector and a Cu-K $\alpha$  sealed tube ( $\lambda = 1.54178$  Å). The sample was scanned in a range between 10° to 70° (2 $\theta$ ), with a step size of 0.02° and an exposure time of 10 s. An SEM (FEI Helios 600 Nanolab FIB-SEM, 3 KV) was used to determine the particle morphology.

The TEM analysis was carried out on a Jeol JEM 2010 microscope fitted with a LaB<sub>6</sub> filament and an acceleration voltage of 200 kV. A combined differential scanning calorimetry/TGA instrument (Mettler-Toledo, TGA/DSC STAR system) was used to study the decomposition and reaction of the precursors.

A description of the method used to prepare the cathode follows. LiV<sub>3</sub>O<sub>8</sub>, Super P conductive carbon, and poly(vinylidene fluoride) (PVDF) binder were mixed at a weight ratio of 70 : 20 : 10, respectively, and then dispersed in a *N*-methylpyrrolidone (NMP) solution to make a slurry. The slurry was coated on aluminium foil and dried in a vacuum oven at 100 °C overnight prior to coin-cell assembly. The Li/LiV<sub>3</sub>O<sub>8</sub> cells (2325 type coin cells, National Research Council, Canada) were assembled in a glove box (Mbraun, Inc.) filled with ultra-high-purity argon using polypropylene membrane (3501, Celgard, Inc.) as the separator, Li metal as the anode, and 1-M LiPF<sub>6</sub> in

ethyl carbonate/dimethyl carbonate (EC/DMC) (1 : 1 EC : DMC v/v) as the electrolyte. The charge/discharge performance of the electrodes and galvanostatic intermittent titration technique (GITT) were evaluated at room temperature using an Arbin Battery Tester BT-2000 (Arbin Instruments, College Station, Texas). For GITT test, the cells discharge or charge 10 min followed by a rest of 40 min in order to obtain the open circuit potentials. The cyclic voltammetry (CV) curves and electrochemical impedance spectroscopy (EIS) were obtained using a CH Instruments Electrochemical Station (CH Instruments, Austin, Texas). The EIS are deducted at 3.5 V vs. Li/Li<sup>+</sup>.

## 3. Results and discussion

### 3.1 Characterization of the thermal co-decomposition process

After commercial V<sub>2</sub>O<sub>5</sub> powder was added to the oxalic acid solution in a stoichiometric ratio of 1 : 3, the color of the liquid changed from yellow to blue, which indicated that the valence had changed from V<sup>5+</sup> to V<sup>4+</sup> and that the vanadium precursor, vanadyl oxalate hydrate (VOC<sub>2</sub>O<sub>4</sub>·*n*H<sub>2</sub>O), had been formed. This reaction can be expressed as follows:



The stoichiometric amount of CH<sub>3</sub>COOLi·2H<sub>2</sub>O then was added to the blue precursor solution, and the precursor mixture was obtained after drying the liquid overnight in air at 80 °C. Fig. 1 shows the TG and DTA results of each individual precursor of VOC<sub>2</sub>O<sub>4</sub> and CH<sub>3</sub>COOLi·2H<sub>2</sub>O, and the precursor mixture under flowing air with a temperature increase rate of 5 °C min<sup>-1</sup>.

The TG/DTA analysis data of CH<sub>3</sub>COOLi·2H<sub>2</sub>O (Fig. 1a) show that, in the temperature range of 30 °C to 100 °C, 5% percent of the mass loss occurs (equivalent to 0.28 water molecule) and an endothermic peak at 57 °C on the DTA curve appear. This result is attributed to desorption of crystallization water that had condensed on the sample surface. Next, a significant mass loss of the sample (30%) is observed between 110 °C and 150 °C (see the TG curve in Fig. 1a). This mass loss, which is related to the dehydration of the remaining 1.72 crystallization water molecules, yields an amorphous CH<sub>3</sub>COOLi. This is corroborated by the peak shown at 126 °C on the DTA curve between 120 °C and 280 °C. Further temperature increases from 150 °C to 360 °C do not result in any mass losses (see the TG curve). The endothermic peak at 285 °C appears on the DTA curve can be attributed to a phase transition. In the temperature range 360 °C to 450 °C, a mass loss caused by thermal decomposition of the amorphous CH<sub>3</sub>COOLi is observed. This loss is confirmed by the presence of two exothermic peaks on the DTA curve at 417 °C and 440 °C, respectively. The first loss is related to carbon combustion at 417 °C after the thermal dissociation of CH<sub>3</sub>COOLi at 385 °C, and the second loss is a major exothermic peak at 440 °C corresponding to the phase transition of highly reactive Li<sub>2</sub>O, which reacts with CO<sub>2</sub> present in the atmosphere of the thermo-analytical furnace. This reaction leads to the formation of Li<sub>2</sub>CO<sub>3</sub>, which is confirmed by the XRD experiment and also manifested by the weight change on the TG curve.

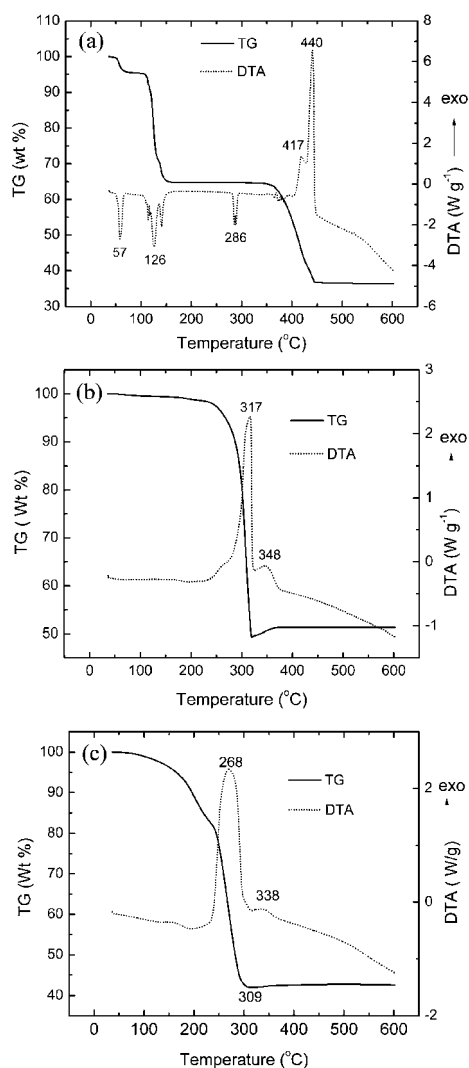


**Fig. 1** TG and DTA results for molar ratio (a)  $\text{CH}_3\text{COOLi}\cdot 2\text{H}_2\text{O}$ , (b)  $\text{VOC}_2\text{O}_4$ , and (c)  $\text{VOC}_2\text{O}_4 : \text{CH}_3\text{COOLi} = 3 : 1$ .

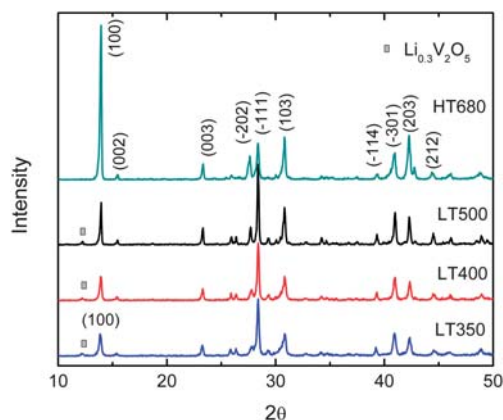
Fig. 1b shows the TG and DTA analysis of  $\text{VOC}_2\text{O}_4$  produced by reacting vanadium pentoxide with oxalic acid in a molar ratio of 1 : 3, followed by drying in air at 120 °C. There is not much weight loss in the temperature range between 30 °C to 267 °C on the TG curve. However, a sharp mass loss follows as the temperature is increased further, and reaches a minimum mass of 49% at 321 °C. This loss is attributed to the decomposition of  $\text{VOC}_2\text{O}_4$  to  $\text{V}_2\text{O}_4$  and the accompanying oxidation of  $\text{V}^{4+}$ . This conclusion is supported by an exothermic peak that occurs at 317 °C. Above 317 °C, the decomposition process is complete; however, oxidation of  $\text{V}^{4+}$  continues, and a slight weight increase is observed on TG curve. According to the TG results, the composition at the bottom of the curve is composed of  $\text{V}_2\text{O}_4/\text{V}_2\text{O}_5$  in a ratio of 1 : 4.

Fig. 1c shows the TG and DTA results for the precursor mixture of  $\text{VOC}_2\text{O}_4$  and  $\text{CH}_3\text{COOLi}$  in a molar ratio of 3 : 1, respectively. In the temperature range between 30 °C and 240 °C, the gradual weight loss is attributed to the water bonded physically and/or chemically to the precursor mixture. A drastic mass loss shown on the TG curve follows as the temperature is further

increased, and a much broader peak at 268 °C and a smaller exothermic peak at 338 °C on DTA curve are observed. According to the mass change, the broad peak is characteristic of thermal co-decomposition of  $\text{VOC}_2\text{O}_4$  and  $\text{CH}_3\text{COOLi}$ . The second small exothermic peak is attributed to the further oxidation of  $\text{V}^{4+}$  to  $\text{V}^{5+}$  in air. As shown in Fig. 1, the decomposition temperature for  $\text{CH}_3\text{COOLi}$  in the composite precursor is lower than that for the pure  $\text{CH}_3\text{COOLi}$  (Fig. 1a). There could be two possible explanations for this thermal co-decomposition. One possible explanation is the large heat energy supplied by the thermal decomposition of another precursor,  $\text{VOC}_2\text{O}_4$ , in the mixture precursor, which can decompose at a lower temperature. Another possible explanation for the lower temperature decomposition of  $\text{CH}_3\text{COOLi}$  is the reaction between  $\text{CH}_3\text{COOLi}$  and  $\text{V}_2\text{O}_5$ , which is produced by *in situ* decomposition of  $\text{VOC}_2\text{O}_4$ . The absence of further peaks on the DTA curve and the constant weight mass on the TG curve (see Fig. 1c) indicate that no further phase transitions and reactions occur.

### 3.2 Structural characterization

The material obtained by heating the precursor mixture in air at 350 °C for 2 h was brown in color, which is the typical color for  $\text{LiV}_3\text{O}_8$ . The XRD patterns for the samples produced using both our thermal co-decomposition method at constant temperature and the conventional high-temperature method are shown in Fig. 2. No differences in peak positions are observed for the samples fabricated at low temperatures (designated as samples LT350, LT400 and LT500). However, the peak intensity, which indicates the high crystallinity of  $\text{LiV}_3\text{O}_8$  in these samples, increases with increasing annealing temperatures. This result corresponds well with the TG and DTA results (see Fig. 1a), which indicate that no further phase transitions and reactions occur above 350 °C. The XRD peak positions for the samples are consistent with the known layered-type  $\text{LiV}_3\text{O}_8$  (JCPDS 72-1193),<sup>28,34</sup> meaning that these  $\text{LiV}_3\text{O}_8$  samples have a monoclinic crystalline structure and belong to the  $P21/m$  space group. It is composed of two basic structural units,  $\text{VO}_6$  octahedron and



**Fig. 2** XRD patterns of  $\text{LiV}_3\text{O}_8$  synthesized using the low-temperature thermal co-decomposition method at various temperatures (350 °C, 400 °C, and 500 °C) in air for 2 h (designated samples LT350, LT400, and LT500, respectively) and  $\text{LiV}_3\text{O}_8$  synthesized using the conventional high-temperature method (at 680 °C for 10 h; designated sample HT680).

VO<sub>5</sub> distorted trigonal bi-pyramids. For all three samples fabricated at low temperature, a Li<sub>0.3</sub>V<sub>2</sub>O<sub>5</sub> impurity phase was detected. This Li<sub>0.3</sub>V<sub>2</sub>O<sub>5</sub> impurity phase has also been observed in LiV<sub>3</sub>O<sub>8</sub> produced by other methods.<sup>10,32,35</sup> Because the amount of Li<sub>0.3</sub>V<sub>2</sub>O<sub>5</sub> is small and it is an intercalation material, it would not have a significant effect on the performance of a LiV<sub>3</sub>O<sub>8</sub> electrode. The XRD pattern of HT680 (as shown in Fig. 2) exhibits much sharper peaks, which suggests a higher degree of crystallinity. Furthermore, the relative intensities of the XRD peaks in these samples are different. The (001) peak is the strongest peak for sample HT680, but the (-111) peak is the strongest peak for samples produced using the low-temperature thermal co-decomposition method (LT350, LT400, and LT500). This difference is attributed to the preferred orientation of the LiV<sub>3</sub>O<sub>8</sub> produced using our low-temperature thermal co-decomposition method, which has nanorod structure.

Fig. 3 shows the morphologies of the LiV<sub>3</sub>O<sub>8</sub> materials prepared using the conventional method (a) and our low temperature thermal co-decomposition method at 350 °C (b–c). As shown in Fig. 3a, the particles in the LiV<sub>3</sub>O<sub>8</sub> prepared using the conventional fabrication method are micro-sized. No space voids are present in the bulk grain particles, although some particles with rod structures appear on the surface of the bulk material. The formation of large particles can be attributed to more kinetically favorable conditions for spontaneous growth of small particles at high temperatures to reduce the surface energy. Fig. 3b and 3c show SEM images of two different magnifications for the nanorod-shaped particles produced by our thermal co-decomposition method at 350 °C. As shown in Fig. 3b, the morphologies of the nanorods are very uniform, and the length of the particles can be as long as several micrometres. The diameters of these nanorods range from 30 nm to 150 nm. Furthermore, the nanorods are well separated, and the space between particles is ample. This kind of structure and particle spacing is advantageous for electrolyte penetration and fast Li<sup>+</sup> ion diffusion because of the nanoscale diffusion distance within

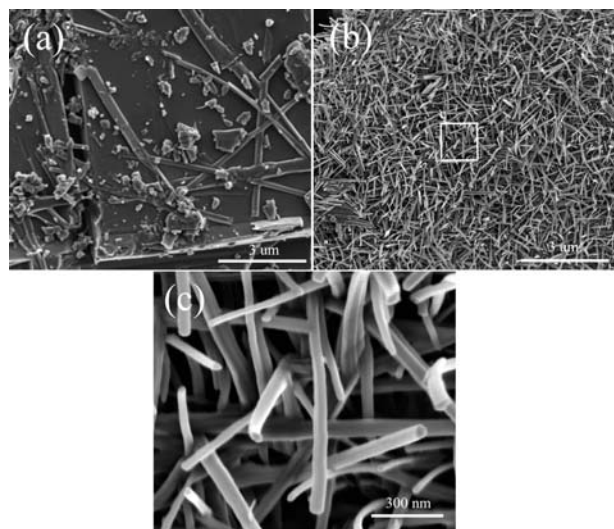


**Fig. 3** SEM images of LiV<sub>3</sub>O<sub>8</sub> prepared using the conventional method (a) and our thermal co-decomposition method at 350 °C in air for 2 h at low (b) and high magnification (c).

the solid state particles. Thus, more active material can be utilized at a high discharge/charge rate, and a high specific capacity can be expected.

The detailed structural features of the nanorods were analyzed using TEM imaging and selected area electron diffraction. Each nanorod is a single crystal as evidenced by the selected area electron diffraction pattern shown in Fig. 4(c). In addition, the TEM images shown in Fig. 4(a) and 4(b) reveal that the nanorod is also populated by stacking fault on the (001) planes, which is also confirmed by the formation of the streaks in the electron diffraction pattern. The nanorod grows approximately along the [-111] direction. It would be expected that the stacking faults could serve as a fast channel for the Li ion diffusion, thus partially accounting for the experimentally better rate capability.

Fig. 5 shows the morphologies of the LiV<sub>3</sub>O<sub>8</sub> particles prepared by our new method at different temperatures. At 350 °C, the nanoparticles are well separated and the morphologies are quite uniform. When synthesized at 400 °C, the nanorod shapes are preserved; however, the particles grow larger, and some of them merge to form a new shape of nanoplate. For the nanoparticles synthesized at 500 °C, the particles grew even larger. This result corresponds well with the XRD results (Fig. 2), which demonstrate higher crystallinity and larger particle sizes at higher temperatures as indicated by its peak intensity and width.

### 3.3. Electrochemical performance

Fig. 6 shows the first cycle CV curves for the HT680 and LT350 LiV<sub>3</sub>O<sub>8</sub> electrodes. During the cathodic scan of sample LT350, the peak at ~2.71 V corresponds to the initial Li<sup>+</sup> ion insertion in the tetrahedral site, and the peak at ~2.41 V is related to further Li<sup>+</sup> ion intercalation into tetrahedral sites with a two-phase transition from Li<sub>3</sub>V<sub>3</sub>O<sub>8</sub> to Li<sub>4</sub>V<sub>3</sub>O<sub>8</sub>. We attribute the last step, which occurs at ~2.24 V, to the slower kinetic insertion process

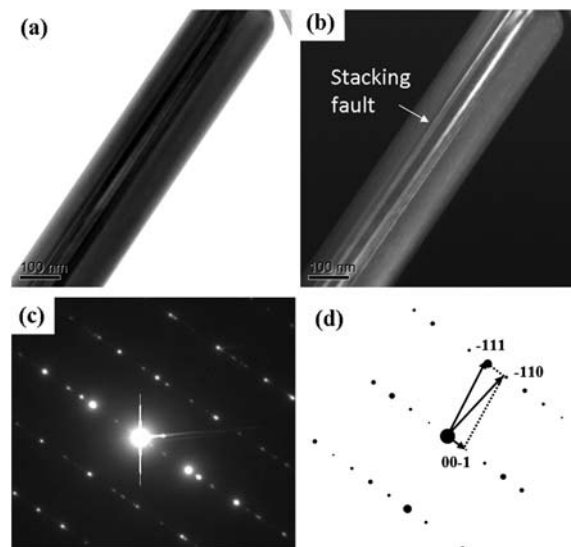


**Fig. 4** TEM images and electron diffraction show the detailed structural nature of the nanorod. (a) Bright field image, (b) dark field image, (c) selected area electron diffraction pattern, (d) calculated electron diffraction pattern with the crystallographic data taken from references 36 and 37.

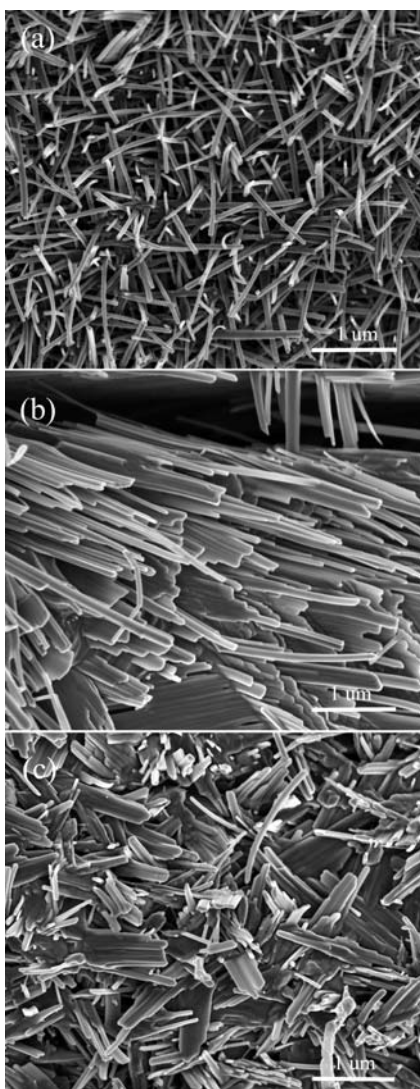


**Fig. 5** SEM images of  $\text{LiV}_3\text{O}_8$  nanorods prepared using our thermal co-decomposition method at constant temperatures of 350 °C (a), 400 °C (b), and 500 °C (c) for 2 h.

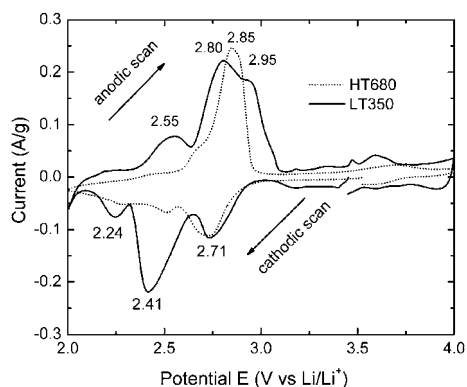


**Fig. 6** The first-cycle CV curves for HT680 and LT350 electrodes.

where the single-phase transition corresponding to the  $\text{Li}_4\text{V}_3\text{O}_8$  phase takes place.<sup>10</sup> As shown in the CV curves of the two electrodes obtained using a different method, a similar current

intensity at a cathodic peak 2.71 V was detected. We believe that this is due to the fast  $\text{Li}^+$ -ion diffusion efficiency in  $\text{LiV}_3\text{O}_8$  for the initial intercalation. In the earlier intercalation stage, many  $\text{Li}^+$ -ion diffusion paths and empty tetrahedral sites are available for  $\text{Li}^+$ -ion occupation between the layers. Even for micro-sized particles, the first  $\text{Li}^+$ -ion intercalation can proceed efficiently. A similar phenomenon was observed by J. Kawatita *et al.*<sup>11,38</sup> at different current densities and different temperatures for the first single-phase transition. However, for the two-phase transition, the peak current density of the LT350 electrode is much higher than that for the HT680 electrode. It has been reported that the diffusion coefficient is much lower for the two-phase transition stage;<sup>38</sup> a possible reason for this difference in diffusion coefficients is that intercalation for the HT680 electrode becomes kinetics limited. However, for the electrode containing  $\text{LiV}_3\text{O}_8$  nanorods prepared using our low-temperature method (shown in Fig. 3), the diameter of the nanorods is <150 nm, so the required  $\text{Li}^+$ -ion diffusion distance is effectively shortened. Furthermore, the existence of large spaces between the nanoparticles can allow easy accommodation of  $\text{Li}^+$  ions during the intercalation process, thus lowering the energy barrier for the diffusion process. This also explains the difference in current density at 2.24 V during the cathodic scan. During the anodic scan, similar behavior is observed. These results demonstrate that  $\text{Li}^+$ -ion diffusion in nanorod-structured  $\text{LiV}_3\text{O}_8$  is more kinetically favorable than diffusion in micro-sized particles.

Fig. 7 shows the discharge/charge curves and cycling performance of the HT680 and LT350 electrodes. As shown in Fig. 7a, a rapid voltage decrease during discharge and a quick voltage increase during charge were observed in the voltage range between 4 V and 2.7 V for the HT680 electrode, followed by a short plateau. Then, a negligible capacity was obtained in this

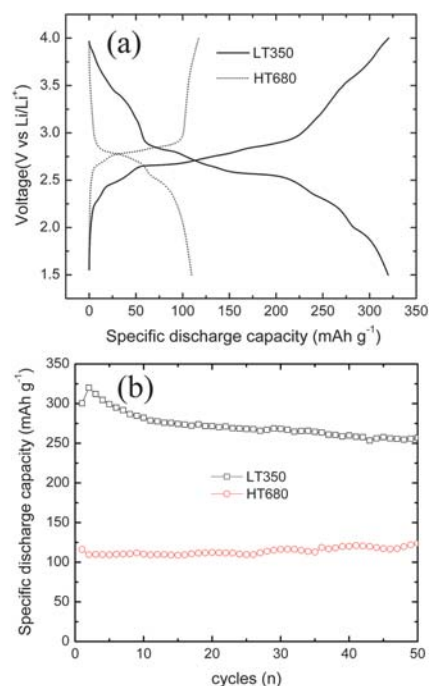


**Fig. 7** Charge-discharge curves (a) and cycling performance (b) of the LT350 and HT680  $\text{LiV}_3\text{O}_8$  electrodes.

voltage range, and the overall specific discharge capacity was only about 109 mAh g<sup>-1</sup> at a current density of 100 mA g<sup>-1</sup>. However, as shown in Fig. 7a, the nanorod electrode (LT350) has more obvious plateaus and higher specific discharge capacity. During the second cycle, it delivers a specific discharge capacity of 320 mAh g<sup>-1</sup>, which is almost two times more than the capacity of the HT680 electrode and also is superior to the best specific discharge capacity result for LiV<sub>3</sub>O<sub>8</sub> prepared using conventional methods (180 mAh g<sup>-1</sup>). Kawakita *et al.*<sup>38</sup> reported that the particle size and shape greatly influence the insertion rate of the crystalline Li<sub>1+x</sub>V<sub>3</sub>O<sub>8</sub>. In our case, the uniform nanorod-structured LiV<sub>3</sub>O<sub>8</sub> electrode is characterized by smaller particle size (<150 nm) and good void space between the particles (shown in Fig. 3b and 3c). This template-free and low temperature synthesized LiV<sub>3</sub>O<sub>8</sub> exhibits both higher capacity and better utilization of the active material.

Fig. 7b shows the cycling performance of the LT350 and HT680 electrodes at a current density of 100 mA g<sup>-1</sup>. The nanorod LT350 LiV<sub>3</sub>O<sub>8</sub> electrode delivers an initial specific discharge capacity of 300 mA h g<sup>-1</sup>, and its capacity reaches 320 mAh g<sup>-1</sup> during the second cycle, which is equivalent to 3.45 mol Li per mol of LiV<sub>3</sub>O<sub>8</sub>. The specific discharge capacity decreases to 282 mA h g<sup>-1</sup> during the tenth cycle and then becomes quite stable in subsequent cycles (*i.e.*, 0.23% capacity fading per cycle between cycles 11 and 100). This capacity fading is a common phenomenon for LiV<sub>3</sub>O<sub>8</sub> electrodes. Guyomard *et al.*<sup>39,40</sup> attributed the capacity fading of LiV<sub>3</sub>O<sub>8</sub> to local damage of the crystal structure caused by the abrupt structural change over the two-phase boundary (occurring around 2.6 V to 2.4 V). In addition, a loss of contact between some grains and the conductive carbon caused by the strong local volume change also is responsible for the capacity fading. In addition, the capacity fading possibly results from the structural change that accompanies reformation of the solid electrolyte interface layer after each cycle. For our electrode, the sample retains a high specific discharge capacity of 256 mAh g<sup>-1</sup> even after 50 cycles. However, the bulk HT680 LiV<sub>3</sub>O<sub>8</sub> electrode exhibited a slight capacity increase during the cycling test. It delivered a relatively low initial discharge capacity of 116 mA h g<sup>-1</sup>, but the discharge capacity steadily increased to 123 mA h g<sup>-1</sup> at cycle 50. Such behavior can be explained by the slight fragmentation of the grains caused by electrochemical grinding during cycling. Because no extra space accompanies the volume change, smaller particles are formed, thus shortening the Li<sup>+</sup>-ion diffusion distance. This behavior also has been reported in the literature;<sup>40</sup> however, the capacity of the HT680 electrode after 50 cycles is still very low compared to the capacity of our sample synthesized at low temperature.

To further understand the improved electrochemical performance, electrochemical impedance spectroscopy and GITT measurements of both samples were performed and the results are shown in Fig. 8. Fig. 8(a) shows the Nyquist plots of LT350 and HT680 materials at 3.5 V. As the electrolyte and electrode fabrication are the same or very similar between the two electrodes, the high frequency semicircle should relate to the resistance of electrode. The resistance of LT350 cells, 50 Ω, is much smaller than 200 Ω for HT680. This result indicates the charge transfer is much improved by our method when comparing to the conventional method of fabricating the material. The nanoscaled materials shortening the electron transportation distance and the

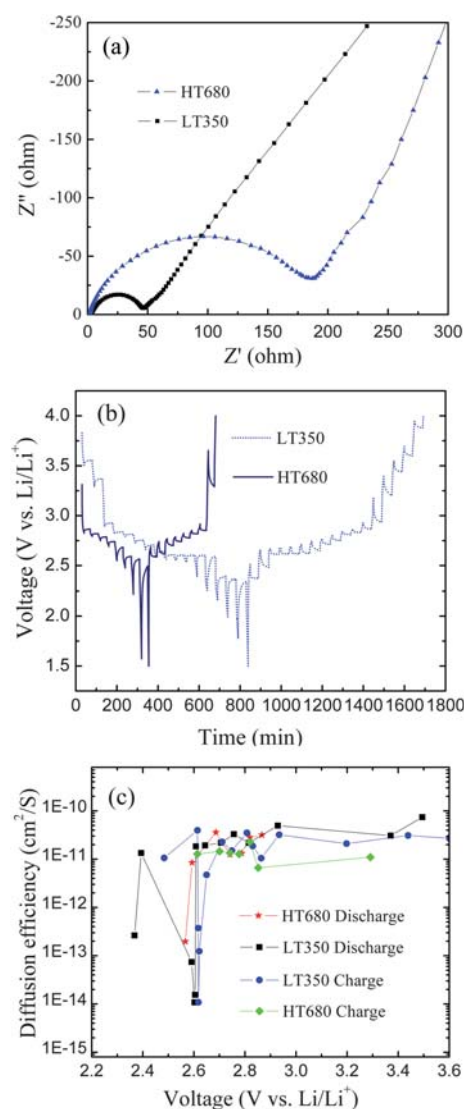


**Fig. 8** Kinetic characterization of LT350 and HT680: (a) Nyquist plot of LiV<sub>3</sub>O<sub>8</sub> at 3.5 V vs. Li/Li<sup>+</sup>; (b) GITT curves during the 11 cycle as a function of time in the voltage range of 1.5–4 V; (c) The Li<sup>+</sup> diffusion coefficients calculated from the GITT curves for both samples as a function of cell voltage during both discharge and charge process.

stacking defaults as shown in Fig. 4 are the two possible reasons for this phenomenon. Fig. 8(b) shows the galvanostatic intermittent titration technique (GITT) curves for both samples after 10 cycles of discharge/charge processes. Both samples were set to discharge (or charge) for 10 min followed by a rest of 40 min in order to obtain the open circuit potential (OCP). It is clearly observed that LT350 experiences more steps than HT680, which is associated with its high capacity. For the calculation of the diffusion coefficients, we adopt the following equation which is also used to determine the Li<sup>+</sup> diffusion coefficients in Li<sub>x</sub>MO<sub>2</sub> (M = (Ni, Co), (Ni, Mn), (Ni, Mn, Co)) and Li<sub>3</sub>V<sub>2</sub>(PO<sub>4</sub>)<sub>3</sub><sup>41–43</sup> as shown below:

$$D_{Li^+} = \frac{4}{\pi} \left( \frac{m_B V_M}{M_B A} \right)^2 \left( \frac{\Delta E_S}{\tau (dE_\tau / d\sqrt{\tau})} \right)^2$$

Where  $V_M$  is the molar volume of the compound,  $M_B$  and  $m_B$  are the molar weight and mass of the host oxide, respectively,  $A$  is the surface area between the electrode and the electrolyte,  $\tau$  is the titration time, and  $\Delta E_S$  the difference of two consequent stabilized open circuit potentials. Fig. 8(c) shows the calculated diffusion coefficients during the discharge and charge processes for both samples. Generally the diffusion coefficient of LT350 is slightly higher than that of HT680 sample. The diffusion coefficient ( $D_{Li^+}$ ) of LT350 sample reaches minima value at the voltage around 2.6 V which corresponds to the discharge and charge plateaus voltages (as shown in Fig. 7(a)). This is related to the two-phase reaction between  $1.5 < x < 3$  of  $Li_{1+x}V_3O_8$ . The change in lattice parameters is larger in  $Li_4V_3O_8$  than in the  $LiV_3O_8$  phase during the lithium ions interaction, and would be the reason for the sharp drops in diffusion coefficient curves. The diffusion coefficient of LT350 sample is lower than that of HT680 sample at  $\sim 2.6$  V. It is probably related to the formation of more  $Li_4V_3O_8$  phase in LT350 sample than in HT680 sample as shown by the fact that the discharge capacity of LT350 is two times higher than that of HT680. Even though the diffusion coefficient of LT350 is shown to be lower than that of HT680 sample, it still has higher discharge and charge capacities than those of HT680. According to Fick's law:  $\tau = L^2/D$ , where  $\tau$  is the required diffusion time,  $L$  is the required diffusion distance of  $Li^+$  ions and  $D$  is the diffusion coefficient of  $Li^+$  ions in the host materials, the required diffusion distance in our case has changed significantly from several micrometre to about 150 nm, thus would be of great advantage to achieve higher power capability.

Fig. 9 shows the electrochemical performance of  $LiV_3O_8$  nanoparticles synthesized at three different temperatures. The highest discharge capacities for  $LiV_3O_8$  electrodes synthesized at 350 °C, 400 °C, and 500 °C are 320 mAh g<sup>-1</sup>, 267 mAh g<sup>-1</sup> and 193 mAh g<sup>-1</sup>, respectively. Between cycles 2 and 100, their capacities fade by 0.23%, 0.27%, and 0.09%, respectively. The specific capacity decreases as the synthesis temperature increases. The particle size and their separation are the reasons for the capacity differences. As shown in Fig. 4, the nanorods are separated very well at relatively low temperature (350 °C), and this structure allows good accessibility of the electrolyte to the active material. At 400 °C, the nanorods begin to merge, leading to a decrease in the void space available for electrolyte diffusion.

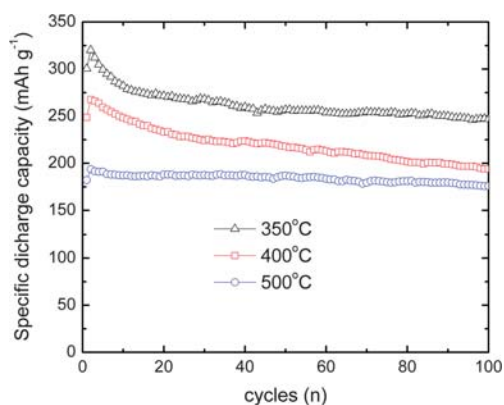


**Fig. 9** Cycling performance of nanorod  $LiV_3O_8$  synthesized at various temperatures.

When synthesized at 500 °C, the particles grow even larger. Because capacity is controlled by the interfacial surface area between the electrolyte and the electrode, the electrode synthesized at 350 °C has a structure more suitable for allowing the nanocrystalline  $LiV_3O_8$  particles to expand freely, thus lowering the energy barrier for  $Li^+$ -ion diffusion. Dunn *et al.*<sup>44</sup> recently reported a similar contribution to the superior electrochemical performance of iso-oriented  $MoO_3$  nanoparticles. In our recent publication,<sup>45</sup> well-separated  $V_2O_5$  also demonstrated superior lithium ion intercalation capability. This also explains why the electrode synthesized at 350 °C has better capacity retention than the electrode synthesized at 400 °C. However, the electrode synthesized at 500 °C has the best capacity retention with a fading rate of only 0.09% per cycle for the initial 100 cycles. One possibility for this phenomenon is its relatively low discharge capacity. Because of the limited  $Li^+$ -ion intercalation into the electrode, the nanosized  $LiV_3O_8$  can accommodate structural changes that occur during the discharge/charge process, although the particle sizes in this electrode are larger than those in the electrodes synthesized at lower temperatures.

Fig. 10 shows the cycling stability of the LT350 electrode at various current densities (*i.e.*, 100 mA g<sup>-1</sup>, 300 mA g<sup>-1</sup>, and 1000 mA g<sup>-1</sup>). The specific discharge capacities of the LT350 electrodes at current densities of 100 and 300 mA g<sup>-1</sup> slightly increase from the first cycle to the second cycle, and reach a maximum during the second cycle. The initial capacity increase is probably related to the wetting of samples during the first cycle. The maximum specific discharge capacities of the LT350 electrodes are 320 mAh g<sup>-1</sup>, 296 mAh g<sup>-1</sup>, and 239 mAh g<sup>-1</sup> for current densities of 100 mA g<sup>-1</sup>, 300 mA g<sup>-1</sup>, and 1000 mA g<sup>-1</sup>, respectively. After 10 cycles, the degree of capacity fading decreases somewhat at various current densities; the capacity fading is 0.23%, 0.30%, and 0.34% per cycle for specific discharge capacities of 100 mA g<sup>-1</sup>, 300 mA g<sup>-1</sup>, and 1000 mA g<sup>-1</sup> between cycles 2 and 100.

The specific discharge capacities of the nanorod  $LiV_3O_8$  samples prepared at low temperatures are much higher than those of the  $LiV_3O_8$ -polypyrrole composite<sup>34</sup> (*i.e.*, 184 mAh g<sup>-1</sup> at a low current density of 40 mA g<sup>-1</sup> for), although the capacity retention of the  $LiV_3O_8$ -polypyrrole composite was found to be good.  $LiV_3O_8$  prepared using the spray-drying technique was

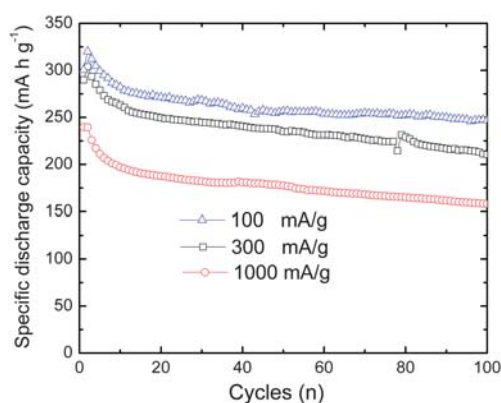


**Fig. 10** Cycling stability of the LT350 electrode at various current densities.

reported to have a high discharge capacity, but it showed a more rapid capacity fading (>2% per cycle) between 2.0 V and 3.7 V.<sup>25</sup> It also demonstrated that our nanorod LiV<sub>3</sub>O<sub>8</sub> performed better than other nanorod LiV<sub>3</sub>O<sub>8</sub> recently reported,<sup>10</sup> which were synthesized using a surfactant-assisted polymer precursor method. The rods synthesized by Sakunthala *et al.*<sup>10</sup> showed good cycle stability and moderate specific discharge capacities of 230 mAh g<sup>-1</sup>, 180 mAh g<sup>-1</sup>, 152 mAh g<sup>-1</sup>, and 75 mAh g<sup>-1</sup> at discharge current densities of 30 mA g<sup>-1</sup>, 120 mA g<sup>-1</sup>, 240 mA g<sup>-1</sup>, and 740 mA g<sup>-1</sup>, respectively. Our nanorod LiV<sub>3</sub>O<sub>8</sub> electrode delivers a high initial discharge capacity of 250 mAh g<sup>-1</sup> and still retains a specific discharge capacity of 158 mAh g<sup>-1</sup> after 100 cycles at a high current density of 1000 mA g<sup>-1</sup>. The superior performance of the nanorods in our work is firstly due to the much smaller rod diameters ranging from 30 to 150 nm when compared to the almost 1 μm diameter of the samples reported by Sakunthala *et al.* Furthermore, the staking defaults as revealed by the TEM images also facilitate the electrolyte penetration and electron transportation, thus would result in better performance. To the best of our knowledge, this is also the best rate performance ever reported for LiV<sub>3</sub>O<sub>8</sub>-based cathode materials, which demonstrates that our nanorod LiV<sub>3</sub>O<sub>8</sub> material is a very promising cathode material for high-rate, secondary-Li-battery applications.

#### 4. Conclusions

We have demonstrated a novel, template-free, low-temperature thermal co-decomposition method for fabricating a nanorod LiV<sub>3</sub>O<sub>8</sub> material. The morphology of the nanorods synthesized at 350 °C is very uniform, exhibiting diameters ranging from 30 to 150 nm and lengths of several micrometres, as well as the defects within the nanorods. Our nanostructured LiV<sub>3</sub>O<sub>8</sub> electrode also exhibits extremely high discharge capacity and excellent capacity retention. A capacity of 320 mAh g<sup>-1</sup> can be achieved at 100 mA g<sup>-1</sup> with only 0.23% capacity fading per cycle. A specific discharge capacity of 158 mAh g<sup>-1</sup> after 100 cycles can be obtained even at a high current density of 1 A g<sup>-1</sup>. These results suggest that the as-synthesized LiV<sub>3</sub>O<sub>8</sub> nanorods are very promising as a cathode material for high-rate secondary lithium batteries.

#### 5. Acknowledgements

We acknowledge the financial support provided by the National Nature Science Foundation of China (No. 50774097), the Creative Research Group of the National Natural Science Foundation of China (No. 50721003), the Laboratory Directed Research and Development Program of Pacific Northwest National Laboratory (PNNL), and the Batteries for the Advanced Transportation Technologies program of Office of Vehicle Technology of U.S. Department of Energy (DOE). The TEM work was performed at the Environmental Molecular Sciences Laboratory, a national scientific-user facility sponsored by the DOE's Office of Biological and Environmental Research and located at PNNL. The DOE Office of Basic Energy Sciences, Division of Materials Sciences and Engineering, also provided support under Award KC020105-FWP12152.

#### References

- 1 M. Armand and J. M. Tarascon, *Nature*, 2008, **451**, 652–657.
- 2 A. Yamada, S. C. Chung and K. Hinokuma, *J. Electrochem. Soc.*, 2001, **148**, A224–A229.
- 3 H. Huang, S. C. Yin, T. Kerr, N. Taylor and L. F. Nazar, *Adv. Mater.*, 2002, **14**, 1525–1529.
- 4 C. Delacourt, P. Poizot, M. Morcrette, J. M. Tarascon and C. Masquelier, *Chem. Mater.*, 2004, **16**, 93–99.
- 5 A. Q. Pan, D. W. Liu, X. Y. Zhou, B. B. Garcia, S. Q. Liang, J. Liu and G. Z. Cao, *J. Power Sources*, 2010, **195**, 3893–3899.
- 6 J. X. Dai, S. F. Y. Li, Z. Q. Gao and K. S. Siow, *J. Electrochem. Soc.*, 1998, **145**, 3057–3062.
- 7 K. West, B. Zschauchchristiansen, S. skaarup, Y. Saidi, J. Barker, I. I. Olsen, R. Pynenburg and R. Loksang, *J. Electrochem. Soc.*, 1996, **143**, 820–825.
- 8 H. Y. Xu, H. Wang, Z. Q. Song, Y. W. Wang, H. Yan and M. Yoshimura, *Electrochim. Acta*, 2004, **49**, 349–353.
- 9 A. D. Wadsley, *Acta Crystallogr.*, 1957, **10**, 261–267.
- 10 A. Sakunthala, M. V. Reddy, B. V. R. Chowdari and P. C. Selvin, *J. Phys. Chem. C*, 2010, **114**, 8099–8107.
- 11 J. Kawakita, Y. Katayama, T. Miura and T. Kishi, *Solid State Ionics*, 2000, **131**, 229–235.
- 12 G. Pistoia, S. Panero, M. Tocci, R. V. Moshtev and V. Manev, *Solid State Ionics*, 1984, **14**, 311–318.
- 13 Q. Shi, L. Z. Ouyang, M. Q. Zeng and M. Zhu, *Electrochem. Commun.*, 2009, **11**, 2169–2172.
- 14 Y. C. Si, L. F. Jiao, H. T. Yuan, H. X. Li and Y. M. Wang, *J. Alloys Compd.*, 2009, **486**, 400–405.
- 15 X. Y. Cao, C. Yuan, L. L. Xie, H. Zhan and Y. H. Zhou, *Ionics*, 2010, **16**, 39–44.
- 16 C. J. Cui, G. M. Wu, J. Shen, B. Zhou, Z. H. Zhang, H. Y. Yang and S. F. She, *Electrochim. Acta*, 2010, **55**, 2536–2541.
- 17 V. A. Zhorin, M. R. Kiselev, T. P. Puryaeva and S. E. Smirnov, *Prot. Met. Phys. Chem. Surf.*, 2010, **46**, 96–102.
- 18 K. P. Lee, K. M. Manesh, K. S. Kim and A. Y. Gopalan, *J. Nanosci. Nanotechnol.*, 2009, **9**, 417–422.
- 19 Y. X. Gu and F. F. Jian, *J. Sol-Gel Sci. Technol.*, 2008, **46**, 161–165.
- 20 L. Liu, L. F. Jiao, Y. H. Zhang, J. L. Sun, L. Yang, Y. L. Miao, H. T. Yuan and Y. M. Wang, *Mater. Chem. Phys.*, 2008, **111**, 565–569.
- 21 X. L. Li, P. P. Li, M. Luo, X. Y. Chen and J. J. Chen, *J. Solid State Electrochem.*, 2010, **14**, 1325–1332.
- 22 H. M. Liu, Y. G. Wang, K. X. Wang, Y. R. Wang and H. S. Zhou, *J. Power Sources*, 2009, **192**, 668–673.
- 23 O. A. Brylev, O. A. Shlyakhtin, A. V. Egorov and Y. D. Tretyakov, *J. Power Sources*, 2007, **164**, 868–873.
- 24 M. Y. Saidi, I. I. Olsen, R. Koksang, J. Barker, R. Pynenburg, K. West, B. Zschauchchristiansen and S. Skaarup, in *Solid State Ionics Iv*, ed., G. A. Nazri, J. M. Tarascon, and M. Schreiber, 1995, 201–209.
- 25 N. Tran, K. G. Bramnik, H. Hibst, J. Prolss, N. Mronga, M. Holzappel, W. Scheifele and P. Novak, *J. Electrochem. Soc.*, 2008, **155**, A384–A389.
- 26 Q. Y. Liu, H. W. Liu, X. W. Zhou, C. J. Cong and K. L. Zhang, *Solid State Ionics*, 2005, **176**, 1549–1554.
- 27 N. Kumagai and A. S. Yu, *J. Electrochem. Soc.*, 1997, **144**, 830–837.
- 28 Y. M. Liu, X. C. Zhou and Y. L. Guo, *J. Power Sources*, 2008, **184**, 303–307.
- 29 T. J. Patey, S. H. Ng, R. Buchel, N. Tran, F. Krumeich, J. Wang, H. K. Liu and P. Novak, *Electrochem. Solid-State Lett.*, 2008, **11**, A46–A50.
- 30 J. G. Xie, J. X. Li, H. Zhan and Y. H. Zhou, *Mater. Lett.*, 2003, **57**, 2682–2687.
- 31 F. Wu, L. Wang, C. Wu, Y. Bai and F. Wang, *Mater. Chem. Phys.*, 2009, **115**, 707–711.
- 32 G. Yang, G. Wang and W. H. Hou, *J. Phys. Chem. B*, 2005, **109**, 11186–11196.
- 33 Y. Zhou, H. F. Yue, X. Y. Zhang and X. Y. Deng, *Solid State Ionics*, 2008, **179**, 1763–1767.
- 34 S. Y. Chew, C. Q. Feng, S. H. Ng, J. Z. Wang, Z. P. Guo and H. K. Liu, *J. Electrochem. Soc.*, 2007, **154**, A633–A673.
- 35 J. Q. Xu, T. Zhang, Q. Y. Pan and Y. H. Gui, *J. Alloys Compd.*, 2008, **467**, 327.



- 36 L. A. de Picciotto, K. T. Adendorff, D. C. Liles and M. M. Thackeray, *Solid State Ionics*, 1993, **62**, 297–307.
- 37 A. D. Wadsley, *Acta Crystallogr.*, 1957, **10**, 261–267.
- 38 J. Kawakita, T. Miura and T. Kishi, *J. Power Sources*, 1999, **83**, 79–83.
- 39 S. Jouanneau, A. L. G. L. Salle, A. Verbaere and D. Guyomard, *J. Electrochem. Soc.*, 2005, **152**, A1660–A1665.
- 40 S. Jouanneau, A. L. G. L. Salle, A. Verbaere, Marc Deschamps, S. Lascaud and D. Guyomard, *J. Mater. Chem.*, 2003, **13**, 921–926.
- 41 K. M. Shaju, G. V. Subba Rao and B. V. R. Chowdari, *J. Electrochem. Soc.*, 2004, **151**, A1324–A1332.
- 42 K. M. Shaju, G. V. Subba Rao and B. V. R. Chowdari, *Electrochim. Acta*, 2003, **48**, 2691–2703.
- 43 X. H. Rui, N. Ding, J. Liu, C. Li and C. H. Chen, *Electrochim. Acta*, 2010, **55**, 2384–2390.
- 44 T. Brezesinski, W. John, S. H. Tolbert and B. Dunn, *Nat. Mater.*, 2010, **9**, 146–151.
- 45 A. Pan, J.-G. Zhang, Z. Min, G. Z. Cao, B. W. Arey, G. Li, S. Liang and J. Liu, *J. Mater. Chem.*, 2010, **20**, 9193–9199.